


Thermoplasmonic Nanomagnetic Logic Gates

Pieter Gypens¹, Naëmi Leo², Matteo Menniti², Paolo Vavassori^{2,3} and Jonathan Leliaert^{1,*}

¹*Dept. of Solid State Sciences, Ghent University, 9000 Ghent, Belgium*

²*CIC nanoGUNE BRTA, Donostia-San Sebastian E-20018, Spain*

³*IKERBASQUE, Basque Foundation for Science, Bilbao E-48009, Spain*

 (Received 22 October 2021; revised 10 June 2022; accepted 1 July 2022; published 4 August 2022)

Nanomagnetic logic, in which the outcome of a computation is embedded into the energy hierarchy of magnetostatically coupled nanomagnets, offers an attractive pathway to implement in-memory computation. This computational paradigm avoids energy costs associated with storing the outcome of a computational operation. Thermally driven nanomagnetic logic gates, which are driven solely by the ambient thermal energy, hold great promise for energy-efficient operation, but have the disadvantage of slow operating speeds due to the slowness and lack of spatial selectivity of currently employed *global* heating methods. As has been shown recently, this disadvantage can be removed by employing plasmon-assisted photoheating, where selective local heating is achieved by the polarization dependence of the optical absorption cross section of the nanomagnet. Here, we show by means of micromagnetic and finite-element simulations how such local heating can be exploited to design reconfigurable nanomagnetic Boolean logic gates. The reconfigurability of operation is achieved either by modifying the initializing field protocol or optically, by changing the order in which two orthogonally polarized laser pulses are applied. Our results thus demonstrate that nanomagnetic logic offers itself as a fast (up to gigahertz), energy-efficient and reconfigurable platform for in-memory computation that can be controlled via optical means.

DOI: [10.1103/PhysRevApplied.18.024014](https://doi.org/10.1103/PhysRevApplied.18.024014)

I. INTRODUCTION

The success of computing in the past decades has been based on the development of charge-based electronics with a von Neumann architecture, which separates the domains of computation and data storage. However, due to the increasing demand in analysis of “big data” in recent years, alternative computation architectures and physical platforms are explored for their potential improvements in energy efficiency and data access [1–3]. Magnetic tunnel junctions [4–6], spin wave conduits [7–10], and magnetic textures such as domain walls [11–14] and skyrmions [15] have been proposed to lie at the basis of computing paradigms to complement current technology that relies on complementary metal oxide semiconductors (CMOSs).

Another promising candidate is nanomagnetic logic (NML), due to its nonvolatility and the potential for low-power operation [16–23]. NML makes use of bistable single-domain nanomagnet islands that encode bits 0 and 1. This state information is communicated to other nanomagnets by magnetic stray fields, which can be tailored by placing the islands in a suitable geometrical arrangement. The fundamental operating principle of a NML gate relies on reaching the logically correct low-energy output

state of the interacting ensemble via a series of successive reversals of the individual nanomagnets [20,24–27]. This principle allowed the implementation of different logical functions, e.g., three-input majority gates [20] and NAND gates [25].

In a conventional approach to computation, nanomagnet reversals are triggered by an external clocking field, which aligns the magnetization of an island along its hard axis [28–33]. This unstable state allows a fast relaxation (down to nanoseconds) into the logically correct low-energy state, which is distinguished by head-to-tail moment arrangements that minimize magnetostatic energy contributions. However, generating the clocking field requires an external power source, and thus comes at an increased energy cost of operation, even though the past decade has seen progress on improving the efficiency of clocked-operation NML, e.g., via the spin-Hall effect [31] or strain-mediated switching [32,33].

Another operation mode for NML relies on *thermally driven* magnetic reversals toward a low-energy state, ideally at ambient temperatures, which could offer energy efficiency near the fundamental Landauer limit [34]. However, the last fifteen years of research have shown that deterministic logic *and* low-power operation via thermal relaxation at room temperature are largely incompatible [35–37]. The trade-off between energy efficiency and

*jonathan.leliaert@ugent.be

reliability stems from the fact that thermally assisted switching requires nanomagnets with low-energy barriers, which is usually achieved by reducing either their size or saturation magnetization. Unfortunately, these modifications go hand in hand with weakening the magnetostatic interactions, which are crucial for logical correctness.

In addition to the drawback of unreliability, the potential advantage of energy-efficient operation of thermally driven NML gates is hampered by slow operation speeds: the time required to obtain the low-energy output state by annealing either at constant temperature [22,24,26,38] or via a cooling protocol [25] is of the order of hours. Furthermore, these heating protocols are *global* and, therefore, lack spatial selectivity to operate more complex logical circuits of hundreds of nanomagnets and impede the integration of NML with CMOS technologies.

To address the problems of reliable and localized operation, it would be advantageous to control the temperature of individual nanomagnets. The selective heating of nanomagnets, thereby lowering their energy barrier while preserving strong dipolar coupling with the neighboring islands, would offer a solution to the problem of having a high energy efficiency *and* reliability, which is necessary to make the concept of NML applicable. Such *local* heating has been reported recently in hybrid ferromagnetic plasmonic nanostructures, where the temperature of individual islands is controlled via the *light polarization* [39].

In this work, we present an operating mode for NML, exploiting local thermoplasmonic heating to engineer a relaxation pathway that guides a NML gate reliably and deterministically toward the low-energy output state, on *nanosecond* time scales. This is illustrated for a reconfigurable AND-OR gate, the design of which is based on a magnetic vertex of four hybrid nanoislands. By means of micromagnetic and finite-element simulations, we demonstrate a high gate reliability and discuss physical considerations for successful gate design. We estimate the optical energy required for a gate operation, yielding a nonvolatile result, in the picojoule range, which is comparable to the costs of writing a bit to a hard drive. Our approach thus combines nonvolatile information storage, optical synchronization, and potential reconfigurability of nanomagnetic logic at nanosecond time scales.

II. PLASMON-ASSISTED OPERATION OF NANOMAGNETIC LOGIC GATES

To enable optically controlled NML, we rely on the concept of thermoplasmonic heating via excitation of localized surface plasmons (LSPs) in metal nanostructures [40], which enable local temperature increases up to several hundreds kelvin [40,41]. Such optical excitations of

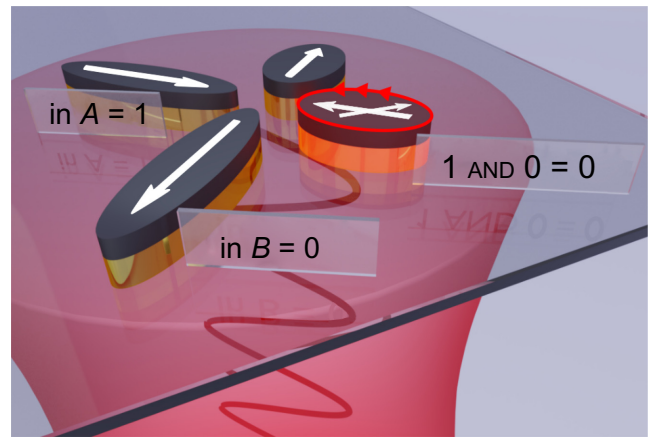


FIG. 1. Reconfigurable thermoplasmonic nanomagnetic AND-OR gate, showing the operational principle of the AND gate. The gate consists of four hybrid nanoislands combining magnetic (gray) and thermoplasmonic (yellow) properties. The linearly polarized laser beam (red, coming from below) only heats the output island (on the right) close to the magnetic Curie temperature via the shape- and polarization-dependent absorption cross section of the plasmonic elements. This selective heating allows for thermally assisted magnetic switching of the output moment toward the logically correct state, as determined by the magnetic configuration of the input moments (A and B).

nanoheaters can be used to promote thermally assisted magnetic switching in hybrid plasmonic nanomagnetic elements [39].

The dependence of the plasmonic heating efficiency on the focal spot position and light polarization [42,43] allows us to implement spatially selective heating schemes, as illustrated in Fig. 1. Here, elliptical thermoplasmonic nanomagnetic hybrid elements of different shape and direction are arranged in a vertex configuration. Because of the orthogonal orientation of the four islands, this design allows us to use the polarization-dependent thermoplasmonic heating to address specific nanomagnets for the logic operation: if illuminated with a short polarized nanosecond laser pulse, and with proper choice of the hybrid element dimensions, only one of the four elements is heated significantly, while the others remain cold, even if the beam diameter exceeds the size of the vertex [39,40].

Using thermoplasmonic heating is therefore ideal to drive NML, as it preserves strong magnetostatic stray fields from the neighboring nanomagnets, which remain cool, but allows one to heat the relevant (output) nanomagnet close to its magnetic Curie temperature T_C to trigger a *deterministic* switching event. The combination of these effects massively increases the chances to drive NML gates into their computationally correct low-energy state, as compared to global heating schemes.

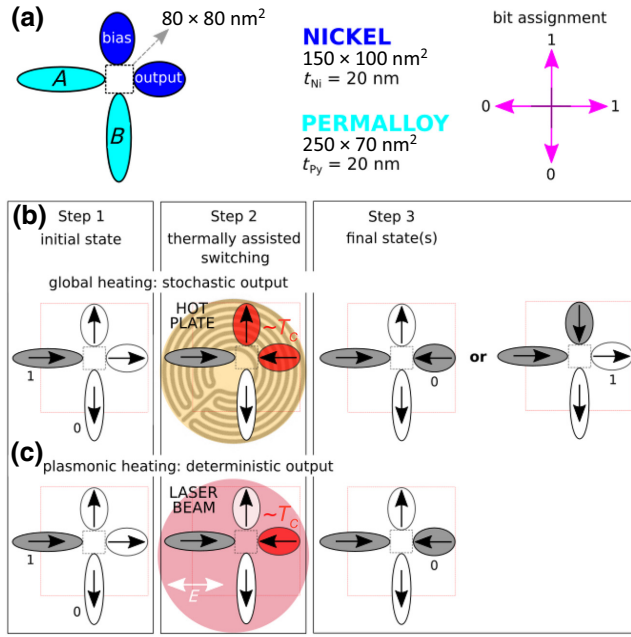


FIG. 2. Gate design and working principle. (a) A thermoplasmonic NML gate consisting of four nanomagnets arranged in a square vertex, similar to the square ASI unit, where bits 0 and 1 correspond to in-plane magnetizations pointing to the left or down and right or up, respectively, as indicated by the pink arrows. The ferromagnetic islands are placed on top of gold plasmonic nanoheaters with a thickness $t_{Au} = 30$ nm. The substrate is made of glass. Because of the higher Curie temperature T_C of permalloy, the input islands (labeled A and B) have a fixed magnetization direction when the gate is heated. (b) In the case of a global heating scheme, either of the bias and output islands is able to reverse (two-headed arrow), yielding two possible vertex configurations of lower magnetostatic energy and thus a stochastic output. (c) Based on the light polarization, thermoplasmonic heating allows for the selective heating of the output island (having its long axis along the beam polarization \vec{E}). This enables deterministic gate operation with one final state as only the output island is heated close to T_C . Islands in gray and white have a magnetic moment pointing in to and out of the vertex, respectively.

III. GATE DESIGN

In the following, we describe the behavior of the simplest possible reconfigurable AND-OR NML gate with four islands, i.e., two input bits, labelled A and B , an output bit, and a bias island. As shown in Figs. 1 and 2, we arrange these in a four-vertex configuration, inspired by a basic building block of square artificial spin ice (ASI), which has a well-known energy hierarchy [44]. As indicated by the pink arrows in Fig. 2(a), bit 0 corresponds to an in-plane magnetization pointing to the left or down, bit 1 to an in-plane magnetization pointing to the right or up.

Materials as well as the sizes and aspect ratios of the hybrid nanoislands have to simultaneously optimize four objectives: to allow for (i) a magnetic field protocol that can set the initial high-energy states, (ii)

polarization-selective thermoplasmonic heating to reverse the magnetization of the bias or output island, without substantially increasing the temperature nor changing the magnetization of the other islands, (iii) magnetostatic interactions that are sufficiently strong to induce the desired logical behavior, and (iv) compatibility with fabrication via state-of-the-art nanolithography. Meeting design objectives (ii) and (iii) is facilitated by using nanoislands consisting of different magnetic materials: by fabricating input islands A and B from permalloy (Py, a nickel-iron alloy with $T_C^{Py} = 843$ K) with high M_s we ensure strong stray fields, whereas the bias and output islands can be switched with less required heating, and thus a smaller beam fluence, to achieve temperatures close to T_C by fabricating them from nickel (Ni, $T_C^{Ni} = 628$ K).

We consider Py input islands A and B with lateral dimensions of 250×70 nm², while the vertical bias island and the horizontal output island are made of nickel with lateral dimensions of 150×100 nm². The thickness of all ferromagnetic islands is equal to $t_{FM} = 20$ nm and the edge-to-edge interisland distance is 80 nm. The ferromagnetic islands incorporate thermoplasmonic heaters made of gold (Au) with a thickness of $t_{Au} = 30$ nm on a glass substrate, which promote LSPs with sharp peaks in the visible spectral region [40,41].

IV. GATE OPERATION

A nanomagnetic computation cycle consists of three steps. First, the input and bias islands have to be initialized in their desired configuration. Second, the NML gate is thermally excited to relax to a suitable low-energy state. Finally, the obtained state is measured. As illustrated in Figs. 2(b) and 2(c), deterministic NML operation in the presented four-vertex gate is only obtained in the case of plasmonic heating for input configuration 10. In the case of global heating, e.g., via a thermal contact with a hot-plate or plasmonic heating with circularly or diagonally polarized light, either the Ni bias or Ni output island can switch. However, global heating does not allow for any control which of the two islands will switch first. The computational outcome, with two more-or-less equally possible vertex configurations, is therefore stochastic [see Fig. 2(b)]. In contrast, shown in Fig. 2(c), the polarization-dependence of plasmon-assisted photoheating allows to heat the output island only, selecting a precise relaxation path and resulting in deterministic computational outcome.

A. Initialization: field protocol

The initialization protocol has to prepare the input bits A and B to their desired state, as well as to ensure that the bias moment is set consistently for the desired logic operation [1 (bias moment pointing up) for the AND operation and 0 (bias moment pointing down) for the OR operation as we discuss later in Sec. IV C and Fig. 5(a)].

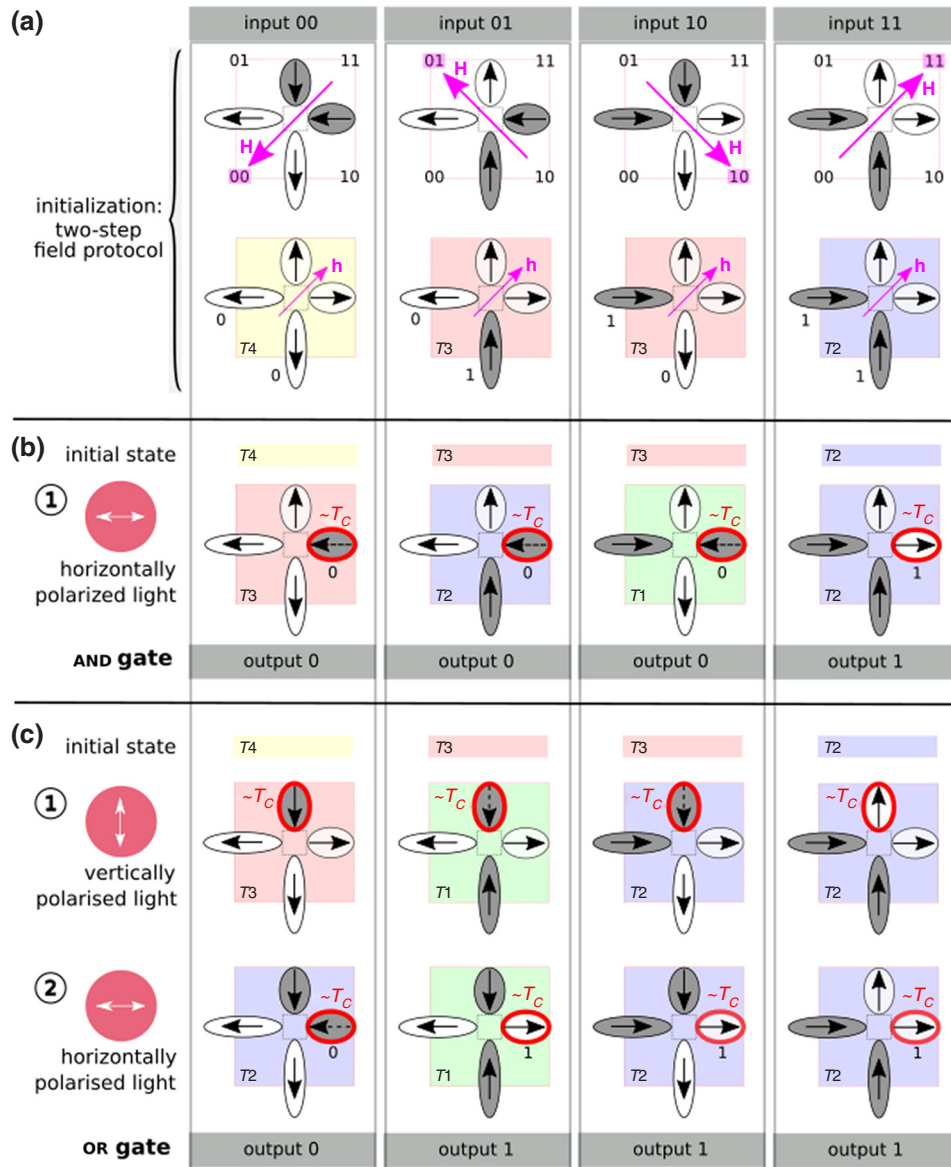


FIG. 3. Operating principle of the proposed reconfigurable thermoplasmonic NML gate, where the states are labeled according to the nomenclature of the energy hierarchy of ASI vertices with $E(T4) > E(T3) > E(T2) > E(T1)$. (a) The first step of the field protocol, shown in the top row, sets the input bits via the saturation with field \vec{H} . In the second step of the field protocol, a smaller field \vec{h} is applied to set the desired orientation of the bias moment. (b) AND logic is induced by irradiating the entire gate with a laser beam of ① horizontally polarized light. Because of the preferential thermoplasmonic heating of the horizontal output island, the magnetization of this island can reverse to a state of lower energy, as indicated by the dotted arrows. (c) OR logic is induced by irradiating the entire gate with a laser beam of ① vertically polarized light (which allows the switching of the vertical nickel island) and thereafter with ② horizontally polarized light (which allows the switching of the output island).

In this work, we consider the two-step field protocol shown in Fig. 3(a). The input islands are initialized by applying a sufficiently large magnetic field \vec{H} along the 00, 01, 10, or 11 direction, depending on the input configuration to be set. The field-saturated state thus obtained is subsequently subjected to a second, smaller, external magnetic field. This field \vec{h} allows us to independently set the magnetization of the nickel bias and output island, as its

amplitude is too small to reverse the magnetization direction of the permalloy input islands. The latter have a larger coercive field, due to the higher aspect ratio (3.6 versus 1.5) and zero-kelvin saturation magnetization (965 versus 615 kA/m [45]). In the example shown in Fig. 3(a), the field \vec{h} is applied diagonally such that it switches the bias moment to point up, and as a consequence, sets the output moment to point toward the right.

It should be noted that this initialization protocol is intended only as an illustrative example (which is convenient to use for lab-based demonstration experiments), and other initialization techniques like spin-polarized current pulses and the spin-Hall effect may be considered as well.

B. Optical selectivity and magnetostatic interactions

The configurations as initialized with the suggested field protocol, or using other initialization procedures, are generally high-energy states following a hierarchy $E(T4) > E(T3) > E(T2) > E(T1)$, where T_i denotes the specific vertex configuration according to the convention used for square ASI [44]—all state configurations and their energies are shown in Figs. 5(a) and 5(b) below.

As shown in Figs. 3(b) and 3(c), the relaxation toward the low-energy state is governed by irradiating the entire gate with a laser beam. Horizontally polarized light predominantly heats the horizontal output island (allowing it to switch when energetically favorable), whereas vertically polarized light will predominantly heat the vertical bias island. By suitable choice of the island's aspect ratio, the input islands are configured to remain cool upon illumination, such that their magnetization remains fixed.

For input configurations 00, 01, and 10, the gate relaxes to the logically correct state, as controlled by the island-selective thermoplasmonic heating. In contrast, no switching occurs for input configuration 11 (fourth column of Fig. 3) because the reversal of the output or bias island would lead to a high-energy $T3$ state. A simultaneous switching event of both nickel islands from the initial $T2$ state directly to the $T1$ ground state is only possible via global heating but unlikely to occur.

To achieve the desired island-selective thermoplasmonic heating, the difference in the polarization-dependent LSP absorption cross sections should be as large as possible for the bias and output islands. Therefore, the long ellipse diameter is set at $d_{\max} = 150$ nm such that the maximum of the plasmonic resonance occurs at a laser wavelength of $\lambda = 728$ nm for light polarization along this axis. The short axis length is mainly determined by the condition that light polarization parallel to this axis should result in a significantly lower LSP energy-absorption efficiency, putting an upper limit on d_{\min} . Using $d_{\min} = 100$ nm, which allows reliable fabrication using nanolithography methods, the absorption cross sections are 4.1×10^{-14} and 0.7×10^{-14} m² for polarization along the long and short axes, respectively (see Appendix A 1 for simulation details).

While the horizontal *output* island gets heated upon illumination, the horizontal *input* island A should remain sufficiently cold to keep its magnetization direction fixed. A similar reasoning applies to the vertical *bias* island and the vertical *input* island B . Therefore, the axes of these input islands are chosen such that the LSP frequency does

not match the frequency of the laser beam, i.e., that they exhibit poor thermoplasmonic efficiency. As detailed in Appendix A 1, the absorption cross section of the 250×70 nm² input island A is equal to 2.3×10^{-14} m² in the case of irradiation along the long axis, which is almost half compared to the output and bias island. The other input island B , having its short axis along the beam polarization, is not heated at all, since the absorption cross section for irradiation along the short axis is 10 times smaller.

In addition, due to the higher Curie temperature of permalloy as compared to nickel (843 versus 628 K), the saturation magnetization of the input islands and hence their switching energy barrier are marginally affected by plasmonic heating; at the maximal light-induced temperature of about 600 K, the decrease of M_s is about only 25% with respect to room temperature [see the temperature profiles of islands A and B shown in Fig. 4(d) below].

The transitions shown in Fig. 3, on which the operation of our gate relies, involve the reversal of an island's magnetization. Such a reversal occurs on a nanosecond timescale when the local temperature of the island approaches its Curie temperature T_C . For a reliable switching event from one state to another, the magnetostatic energy of both states must remain substantially different close to T_C such that the transition probabilities are highly asymmetric, in the sense that only the transition from the high-energy to the low-energy state can take place.

Therefore, our gate is designed to have sufficiently strong magnetostatic interactions, by setting the thickness at $t_{\text{FM}} = 20$ nm to enlarge the magnetic volume, by placing the islands close with an edge-to-edge interisland distance of 80 nm, and by using input islands made of permalloy because of its high saturation magnetization. Since the bias or output island is heated up to T_C , its saturation magnetization almost vanishes, making it less relevant for yielding strong interactions.

C. Operational reconfigurability

Employing the field protocol of Fig. 3(a) and a horizontally polarized light pulse ①, our gate displays the behavior of a logical AND gate [Fig. 3(b)]. However, the same gate design can be used as a logical OR gate by altering the second step of the field protocol, with the small external field \vec{h} pointing to the bottom right instead of the top right, such that the magnetization direction of the vertical bias island is initialized downward instead of upward, yielding $T3$, $T1$, $T2$, and $T3$ as the initial states for input configurations 00, 01, 10, and 11, respectively. These states are then subject to horizontally polarized light, allowing the magnetization of the output island to reverse from right (\rightarrow) to left (\leftarrow) when energetically favorable. The transition occurs for input configuration 00 ($T3 \rightarrow T2$), but not for input configuration 01 ($T1 \rightarrow T3$), input configuration 10 ($T2 \rightarrow T3$), and input configuration 11 ($T3 \rightarrow T4$). As

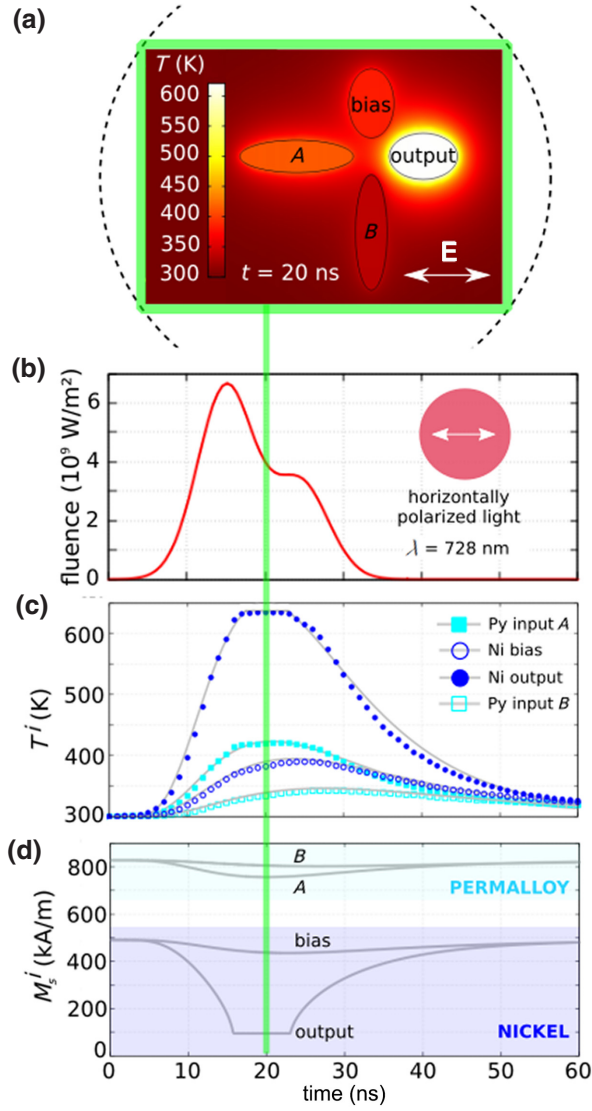


FIG. 4. Time-dependent thermoplasmonic heating. (a) The temperature of the gate $t = 20$ ns after the start of the laser pulse with light polarization \vec{E} along the horizontal direction (white arrow), focused on a nearly diffraction limited two-dimensional Gaussian spot of $1 \mu\text{m}$ FWHM diameter, as indicated by the dashed line. (b) Beam fluence as a function of time when applying two Gaussian laser pulses of 7.8 mW. The horizontally polarized light pulses, with wavelength $\lambda = 728$ nm, are 8.5 ns FWHM and separated by 9.5 ns. The amplitude of the second pulse is only 40% compared to the first pulse. (c) The temperature of each island as a function of time due to the applied laser pulses (symbols). A log-normal distribution has been fitted to the data (solid lines). (d) The saturation magnetization of each island as a function of time.

a result, only input configuration 00 gives rise to output 0, in accordance to a logical OR gate.

As shown in Fig. 3, reconfigurability can also be achieved in an optical manner, which is particularly advantageous to dynamically reprogram the logical operation

even after its initialization. The light protocol determines whether the gate displays the behavior of a logical AND gate [Fig. 3(b)] or a logical OR gate [Fig. 3(c)]. The magnetization of the output island settles into a direction that is consistent with AND logic by applying a horizontally polarized light pulse ① [Fig. 3(b)]. In contrast, as shown in Fig. 3(c), OR logic is observed in the case of a vertically polarized pulse ① followed by a horizontally polarized pulse ②. Thus, while it suffices to apply a single pulse to induce AND logic, the OR gate requires the subsequent application of both light polarizations. Considering the energy of operation and speed for an individual gate, it is therefore beneficial to use the field reconfigurability to induce OR logic, in which case only one pulse is needed.

V. GATE PERFORMANCE

A. Simulations

We use COMSOL Multiphysics[®] [46] to calculate the absorption cross sections and to model the light-induced temperature increase in the hybrid ferromagnet-heater nanostructure [Fig. 4(a)], as detailed in Appendix A 1 and Appendix A 2.

The light pulses can be described as the sum of two Gaussian light pulses, each one of 8.5 ns full width at half maximum (FWHM) and separated by 9.5 ns, as shown in Fig. 4(b). The amplitude of the second pulse is only 40% compared to the first pulse, where the pulse energy of the latter is equal to 63 pJ (yielding a net pulse energy of 88 pJ). This double-pulse excitation at a wavelength of $\lambda = 728$ nm is chosen to obtain a temperature profile in which only the output island is heated close to its Curie temperature T_C and remains at this temperature for a time of about 10 ns, as shown in Fig. 4(c). This enables sufficient time for the nickel output island to reliably switch. A log-normal distribution, cut-off at the Curie temperature of the nickel output island ($T_C^{\text{Ni}} = 625$ K), is fitted to the temperature profile $T^i(t)$ of each island, with i denoting the A , B , bias, or output islands.

These fitted temperature profiles $T^i(t)$ are used to describe the time evolution of the respective saturation magnetization $M_s^i[T^i(t)]$ in the micromagnetic simulation program MuMax3 [47,48], which numerically solves the stochastic Landau-Lifshitz-Gilbert equation. The saturation magnetization is equal to [39,49]

$$M_s^i[T^i(t)] = M_0^i [1 - T^i(t)/T_C^i]^{0.35}, \quad (1)$$

and displayed in Fig. 4(d) for each of the four islands. We use the Curie temperature $T_C^{\text{Py}} = 843$ K for the permalloy islands ($i = A, B$) and $T_C^{\text{Ni}} = 628$ K for the nickel islands ($i = \text{bias, output}$). The values used for the saturation magnetization at zero kelvin are $M_0^{\text{Py}} = 965$ kA/m

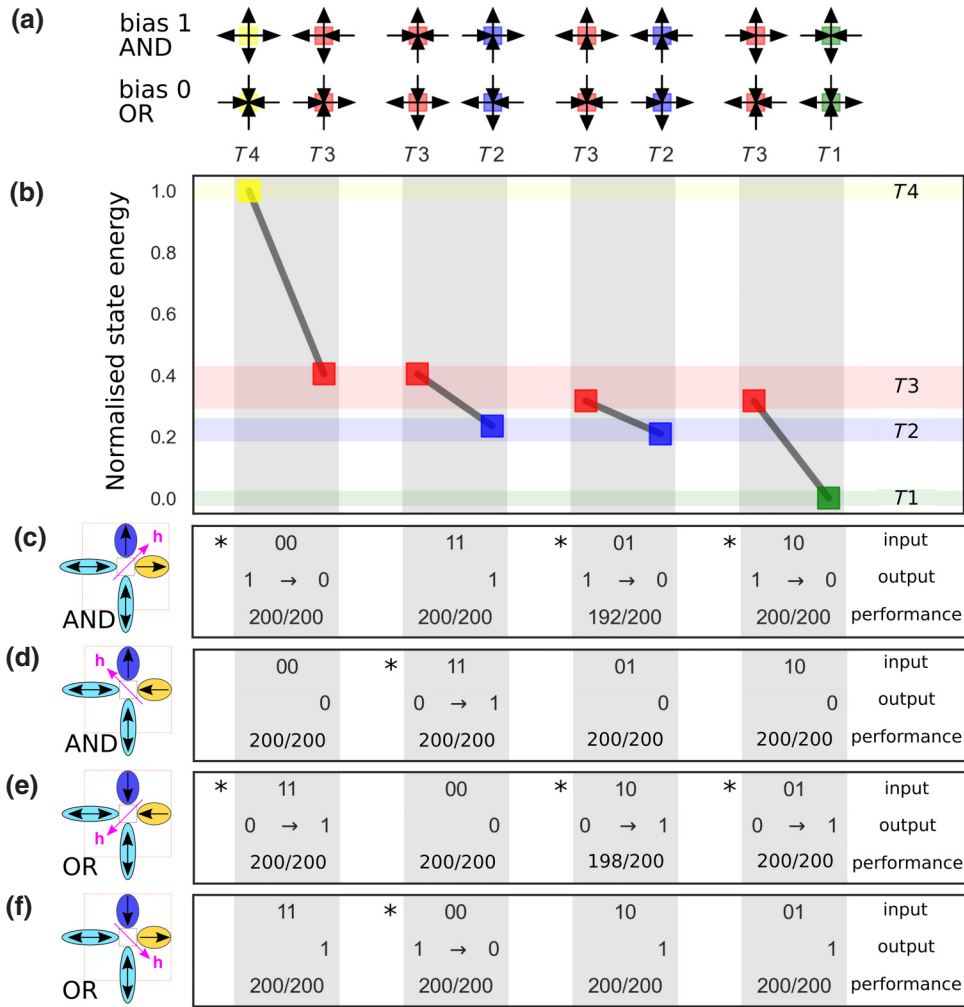


FIG. 5. Energy hierarchy and gate operation. (a) Sixteen possible spin configurations, with the bias island set to 1 (\uparrow , top row) or 0 (\downarrow , bottom row). (b) The normalized magnetostatic state energies (at $T = 300$ K) result in an energy hierarchy $E(T4) > E(T3) > E(T2) > E(T1)$. (c),(d) The logic table for the AND gate for different input configurations, with the bias island set to 1 by the field \vec{h} and the output island to 1 and 0, respectively. The correct output is either obtained from a switching event (e.g., 1 to 0) or by the system remaining in a low-energy state. The last row gives the performance of the simulated gate, i.e., the success rate at which the correct operation (switch or stay) is observed. The operation (switch versus stay) is reversed for both AND gates, as indicated by the asterisks. (e),(f) Equivalent logic table for the OR gate, with the bias island set to 0 by the field \vec{h} and the output island to (e) 0 and (f) 1. These gates are related to the AND gates in (c) and (d) by a global reversal symmetry ($0 \leftrightarrow 1$).

for permalloy ($i = A, B$) and $M_0^{\text{Ni}} = 615$ kA/m for nickel ($i = \text{bias, output}$) [45]. Plots of the saturation magnetization of nickel and permalloy as a function of temperature can be found in Appendix A 3.

Our gate design, shown in Fig. 2(a), is discretized in cells of $5 \times 5 \times 10$ nm³, where we only explicitly include the magnetic part of the design in the micromagnetic simulations. The damping constant is set at $\alpha = 0.02$, the exchange stiffness at $A = 1.3 \times 10^{-11}$ J/m, and the magnetocrystalline anisotropy constant at $K = 0$.

To investigate the performance of our gate, we check whether the magnetization of the output island is oriented along the desired direction after applying a horizontally polarized light pulse (i.e., at $t = 100$ ns). Each

input configuration is tested 200 times, with the magnetization direction of the vertical bias island initialized upward and downward to recover logical AND and OR behaviors, respectively, to demonstrate the reconfigurability of our gate. In addition, to reveal underlying symmetries, we initialize the output either at bit 1 (by applying the small external field \vec{h} in the second step of the field protocol pointing diagonally to the upper or lower right) or at bit 0 (by applying \vec{h} diagonally to the upper or lower left). Figures 5(c)–5(f) show all of the four possible gate initializations with respect to the state of the bias and output island. In our micromagnetic simulations, these initial states are set directly instead of via a field protocol for the sake of simplicity.

B. Results

The performance of the simulated gates, i.e., the success rate of the logically correct operations, is determined by the energy difference between the involved states. In the case of a pronounced energy difference (first, second, and last columns of Fig. 5), the performance is always 200/200. However, for a smaller energy difference (third column), the performance depends on whether a reversal of the output island is required in order to obtain the desired logical behavior, as indicated with the asterisks.

Although the energy difference is the same for AND 01* and AND 01 [see the third column of Figs. 5(c) and 5(d)], the performance is slightly worse when a switching event has to occur (192/200 versus 200/200). The symmetry breaking is explained by the *ringing effect* that takes place after a reversal. Because of this rotational inertia effect, the final state oscillates about the minimum energy for some time. As a consequence, the energy difference with the high-energy state, which is already very small for this input configuration, momentarily reduces, making it more likely to switch back to the logically incorrect high-energy state.

In Fig. 5, the AND gates shown in panels (c) and (d) are related to the OR gates of panels (e) and (f), respectively, by a global reversal symmetry, which allows us to convert an AND gate into an OR gate and vice versa [25]. When reversing all of the magnetic moments (bits), the magnetostatic energy remains unchanged, as it scales as $|\vec{m}|^2$. Therefore, the performance of such globally symmetric gates is expected to be identical. As verified with micromagnetic simulations, the observed success is the same, except for AND 01* (192/200) and OR 10* (198/200), for which the difference of events can be explained by Poisson statistics [50].

C. Discussion

Because of the symmetries relating the AND-OR system, we can restrict the discussion to the AND gate shown in panel (c) of Fig. 5 without a loss of generality.

The performance of our gate is determined by the time it takes for the output island to reverse its magnetization. The temperature profile shown in Fig. 4(b), where the temperature of the output island remains sufficiently high for only 10 ns, dictates that the magnetic switching needs to take place at the same time scale if the logical behavior requires such a transition. To determine the switching time and to understand the relevant underlying physics, we use a simplified model in which transitions occur via a coherent reversal. This model is validated by the spatially resolved micromagnetic simulations (see Fig. 10 in Appendix A 4).

For a transition in which the states are separated by an energy barrier E_{bar} , the switching time can be expressed by an Arrhenius law as

$$\tau_s = \tau_0 \exp\left(\frac{E_{\text{bar}}}{k_B T}\right) \quad (2)$$

with k_B the Boltzmann constant and $\tau_0 = 1/(2f_0)$ the inverse of twice the attempt frequency [51]. In the case of nanomagnetic islands with uniaxial anisotropy, τ_0 equals [52]

$$\tau_0 = \frac{1 + \alpha^2}{2\alpha\gamma} \sqrt{\frac{\pi M_s^2 k_B T}{4K_u^3 V}}. \quad (3)$$

In this equation, V is the ferromagnetic volume of the island, and γ stands for the gyromagnetic ratio. The uniaxial anisotropy constant is determined as $K_u = E_0/V$, where E_0 denotes the energy barrier of an isolated island, which can be estimated as the energy difference between a state with magnetization along the geometrically short (magnetic hard) axis and a state with magnetization along the geometrically long (magnetic easy) axis. Because of the temperature dependence of M_s and E_0 , the value of τ_0 varies upon illumination, ranging from approximately 10^{-10} s (lowest temperatures) to 10^{-8} s (highest temperatures). However, the exponential dependence of τ_s on the energy barrier greatly overshadows the temperature dependence of τ_0 , allowing us to neglect this effect on the total switching rate.

The energy barrier that must be overcome in the transition from state i to state j can be calculated with the mean-field barrier method [53] as

$$E_{\text{bar}}^{i \rightarrow j} = E_0 + \frac{1}{2}(E_{\text{ms}}^j - E_{\text{ms}}^i) \quad (4)$$

with E_{ms} the time- and temperature-dependent magnetostatic energy. In Fig. 6, the energy barriers related to the transitions of our AND gate are shown as a function of time. Note that the mean-field energy barrier can be negative [see Figs. 6(a) and 6(c)]. In this case, the transitions do not involve a potential well into which a state can be trapped, but should be interpreted as barrierless, where a larger negative value corresponds to a more likely transition.

Equations (2)–(3) allow us to determine when the switching time is less than 1 ns. On this time scale, we expect that switching is likely to occur, since the temperature of the output island is close to T_C for a period of 10 ns. However, in some cases, e.g., the AND gate with input configuration 01 [see Fig. 6(b)], the switching times well exceed the 1 ns limit in the entire time window, although our micromagnetic simulations have shown that these transitions do take place.

The discrepancy between the switching time obtained by the mean-field barrier, which makes a reversal unlikely, and the micromagnetic simulations of switching events can be explained by the fact that the energy barrier used in the mean-field barrier method is independent of the magnetostatic energy of transient states, i.e., whether the magnetization rotates clockwise or counterclockwise. It has been shown that the energy barrier for clockwise and

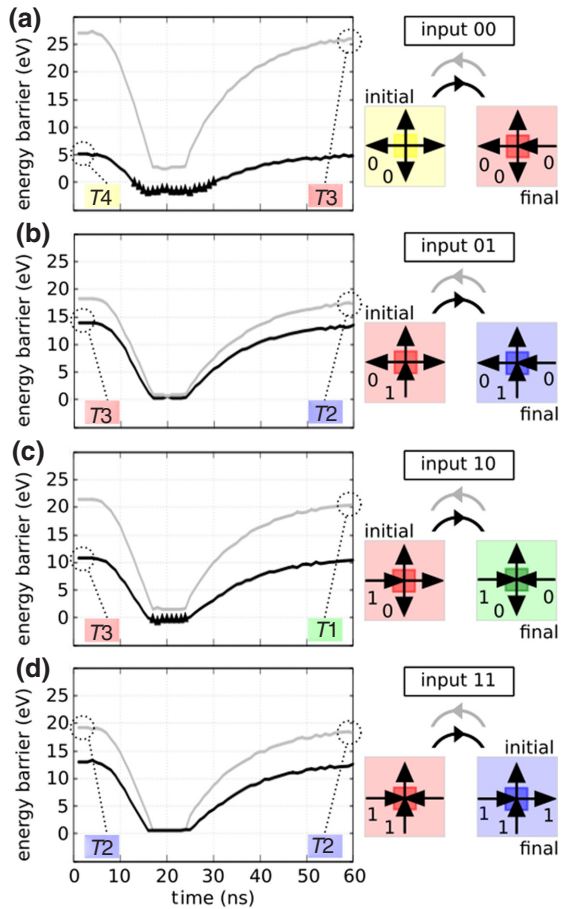


FIG. 6. Overview of the transitions that can take place during the operation of our AND gate, with input configurations (a) 00, (b) 01, (c) 10, and (d) 11. The mean-field energy barriers are determined via Eq. (4) and can therefore become negative, as is the case in panels (a) and (c). The black triangles indicate when the switching time τ_s from Eq. (2) is below 1 ns, for which switching is likely to occur. For input 01 [panel (b)], the switching times well exceed the 1 ns limit, although our simulations have shown that these transitions do take place.

counterclockwise rotation can differ due to the magnetic environment, leading to enhanced transition rates [53,54].

Therefore, as shown in Figs. 7(a)–7(d), we calculate the magnetostatic energy of all of the transient states, based on the assumption that the nanomagnets feature quasiuniform magnetic order upon reversal (see Fig. 10 in Appendix A 4). In this calculation, the input and bias islands are assumed to be uniformly magnetized along their long axis, while the uniform magnetization of the output island is set at an angle θ with respect to its easy axis, with θ ranging from -180° to $+180^\circ$ in steps of 1° . Because of the time dependence of the saturation magnetization [see Fig. 4(c)], the energy profiles $E(\theta)$ change as a function of time. The profiles relevant to understand the observed switching events correspond to a time of about 20 ns, since the temperature of the output island then reaches a maximum,

as shown in Fig. 4(b). Based on the energy profiles of Figs. 7(a)–7(d), we are able to explain the performance of our AND gate, in particular why input configuration 01 can give rise to an erroneous output.

For input configuration 01 of our AND gate (Fig. 7), the energy profiles become monotonic functions, instead of having two minima that are separated by a well-defined barrier. Therefore, it is no longer meaningful to use the Arrhenius law of Eq. (2) to determine the switching time τ_s . In the case of vanishing energy barriers, the switching time matches the time scales on which the magnetization dynamics takes place, i.e., the precession frequency. As this zero-barrier regime is maintained for several nanoseconds, the desired transitions are likely to occur. However, during that time scale of vanishing switching barriers, the moment can return to its original orientation due to a subsequent switching event (*ringing*, as above).

The probability of these accidental “erasures” depends on the energy difference ΔE between the high-energy state and the low-energy state. For input configuration 01 [Fig. 7(b)], this energy difference is low and therefore gives a higher error probability. As illustrated in Fig. 7(f), the magnetic moment of the output island, initially pointing to the right ($m_x = 1$), does not reverse reliably to $m_x = -1$, thus yielding a nonzero error probability (red line). For input configurations 00 [Fig. 7(e)] and 10 [Fig. 7(g)], in contrast, the horizontal component of the output moment always reverses to $m_x = -1$, as desired for output 0.

The performance of our gate for input configurations 00 and 10 is enhanced by the fact that the energy profiles for reversal of the output moment via clockwise (gray) and counterclockwise (black) rotation are nearly identical [Figs. 7(a) and 7(c)]. This means that both transition paths coexist, hence increasing the total switching probability by a factor 2. For input configuration 01, in contrast, a pronounced difference between clockwise and counterclockwise rotation is observed [Fig. 7(b)]. This is because the vertical islands both have a magnetization pointing up, giving rise to a net magnetic field with which the magnetization of the output island tends to align. Thus, the clockwise rotation, in which the magnetization of output island opposes this field, results in a higher-energy barrier. As a result, the counterclockwise rotation is the predominant switching mechanism for input configurations 01 [Fig. 7(b)] as well as 11 [Fig. 7(d)], with the latter not requiring a switching event for the logically correct output.

The above claim on the transition paths (clockwise or counterclockwise rotation) is supported by Figs. 7(i)–7(l), which show how the vertical component of the magnetic moment of the output island, m_y , evolves in time. For input configuration 01 [Fig. 7(j)], m_y is skewed toward positive values. In contrast, for input configurations 00 and 10 [Figs. 7(i) and 7(k)], it oscillates between $m_y = -1$ and $m_y = 1$. Note that the frequency of the oscillatory behavior, which can be considered as the attempt

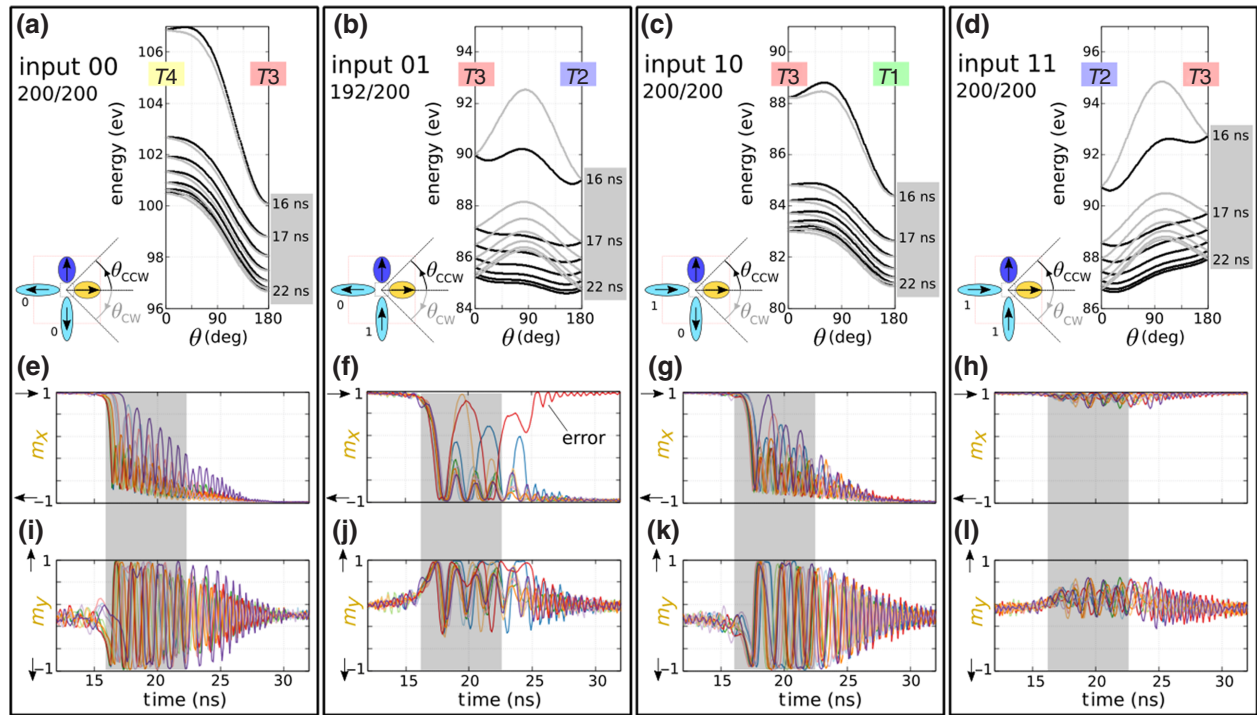


FIG. 7. Relationship between the energy profile and the magnetic moment of the output island. (a)–(d) Static energy profiles $E(\theta)$ of our AND gate for a clockwise (CW, gray) and counterclockwise (CCW, black) reversal of the output island, displayed at times between 16 and 22 ns for which the output temperature is maximal. The energy profiles estimate the variation of the switching barriers during the thermoplasmonic heating cycle. In the case of input 01, shown in (b), the energy profiles become almost monotonic for counterclockwise rotations, and thus allow potential back-switching events. Panels (e)–(h) and (i)–(l) show the simulated time evolution of the horizontal and vertical components of the magnetic moment of the output island, respectively. The results are shown for ten equivalent micromagnetic simulations run with different realizations of the thermal fluctuations.

frequency, is larger for input configuration 00 (approximately 2 ns) than for input configuration 10 (approximately 1 ns) due to the larger slope of $E(\theta, T)$.

Our micromagnetic simulations thus show that the gate performance can reach 100% in the case of a pronounced energy difference between the logically correct and incorrect states at elevated temperatures (i.e., when the temperature of the output island is close to T_C and switching events can take place). This is always the case, except for input configuration 01, for which the AND gate has a 96% performance (192/200). An improvement in the performance is achievable by increasing the energy difference between the logically correct and incorrect states. In this regard, a promising path to explore is the deformation of the vertex from square to rectangular [55,56]. An alternative is to use a bias island made of permalloy instead of nickel, albeit at the cost of revoking the reconfigurability via the light polarization.

VI. CONCLUSION

In this work, we discuss how the vertex of a square ASI, consisting of hybrid nickel-gold and permalloy-gold

islands, can function as a NML gate by taking advantage of light-induced polarization-dependent (and thus island-specific) heating. The operating speed of our thermoplasmonic NML gate exceeds that of a globally heated, thermally driven NML gate, since the switching events take place at nanosecond time scales. The optical energy costs of operation, of the order of 100 pJ for the specific laser considered here, is furthermore on par with the energy costs of writing bits to a commercial hard disk drive or solid-state drive, which is estimated to be of the order of 10 nJ/bit [57]. Thus, our gate has a technologically attractive operating speed, just like clocked NML gates, and combines this advantage with the high energy efficiency of thermally driven gates.

Furthermore, our thermoplasmonic NML gate is reconfigurable between AND logic and OR logic operations, either by reversing the initial magnetization direction of the bias island with an applied field, or optically, by changing the order in which horizontally and vertically polarized light illuminates the gate.

Although the potential of optical reconfigurability of the gate operation has not been fully exploited in this work—there are only a limited number of transitions that can take place in our simple single-vertex gate—it can be

a powerful tool in more complex gate designs. Designing such gates is significantly simplified when compared to conventional NML gates, since it can be delegated to a screening process that only requires knowledge of the field-set initial states and a choice of thermoplasmonic excitation pulses, instead of needing to explore the entire energy landscape of the interacting ensemble to account for stochastic switching events. By using such a simple approach, we present a possible design of a functionally complete NAND gate in Appendix A 5.

The benefits of optical reconfigurability reach their full potential for more complex NML gates, as the light protocol allows one to select a specific relaxation path that in turn determines the logical behavior of the gate. Furthermore, optical degrees of freedom to control the nanomagnetic relaxation offer additional advantages, such as *in-operando* reconfigurability [as demonstrated in Figs. 3(b)–3(c)], the use of light polarization and power to encode analogue information, as well as distributed and parallel operation by using shaped light beams. These advantages offer themselves to be explored for non-Boolean computation, such as reservoir computing in ASI [58–62], as well as stochastic and probabilistic computing schemes [63–65]. We therefore envision future research will focus on in-memory computing in gates that are reconfigurable in a way that cannot be achieved with conventional clocking fields.

ACKNOWLEDGMENTS

J.L. received support from a Fonds Wetenschappelijk Onderzoek (FWO-Vlaanderen) Senior Postdoctoral Research Fellowship (12W7622N). N.L., M.M., and P.V. acknowledge support from the Spanish Ministry of Science, Innovation and Universities under the Maria de Maeztu Units of Excellence Programme (CEX2020-001038-M) and the predoctoral Grant PRE2019-088070 (M.M.), as well as from the Spanish Ministry of Science, Innovation and Universities and the European Union under project RTI2018-094881-B-I00 (MICINN/FEDER). The work of N.L. was supported via the European Union’s Horizon 2020 research and innovation programme under the Marie Słodowska Curie Grant Agreement No. 844304 (LICONAMCO).

APPENDIX

1. COMSOL details and absorption cross sections

The spectral dependence of the absorption cross section of the Au-FM elliptical nanostructures on glass are computed with the “wave optics” module of COMSOL for wavelengths in the visible to near-infrared spectrum (i.e., 400–1200 nm), and following the method described in Ref. [42]. We use the geometrical ellipse dimensions given in Sec. III of the main text, i.e., $150 \times 100 \text{ nm}^2$ for the bias

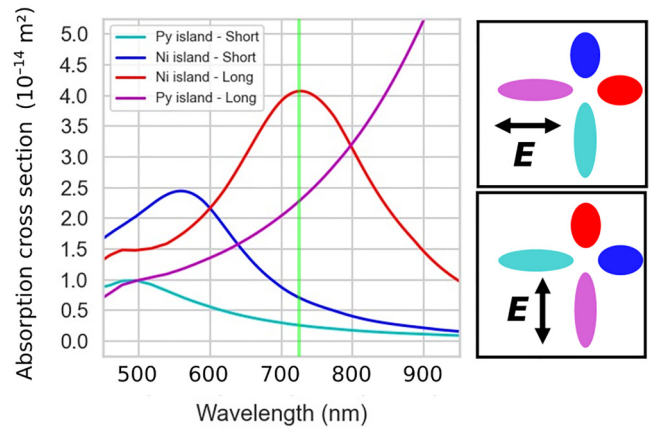


FIG. 8. Calculated absorption cross-section spectra for the Au/Ni (red and blue) and Au/Py (magenta and cyan) hybrid magnetic plasmonic nanoislands with light polarization \vec{E} , as indicated by the arrows. The maximum absorption in the Ni nanoislands (output and bias) is obtained when the wavelength of the light is $\lambda = 728 \text{ nm}$, as indicated by the green vertical line.

and output island and $250 \times 70 \text{ nm}^2$ for the inputs, with the height being set to 20 and 30 nm for Ni/Py and Au, respectively. The islands are embedded in a medium with refractive index $n = 1.2$, an average for the glass and air [42]. We use tabulated optical constants (i.e., wavelength-dependent refractive indices) taken from Ref. [66] for gold and from Ref. [67] for nickel and permalloy via Ref. [68].

The calculated absorption cross section for the nanoislands with the light polarized horizontally is shown in Fig. 8. To maximize the absorption displayed by the output island when the light is polarized along the island’s long axis, the wavelength of the light should be $\lambda = 728 \text{ nm}$. For experimental implementation of the gate, the position of the LSP absorption peak can be tuned by changing the material of the islands plasmonic layer and the thickness. Parasitic heating of the input island can be reduced by replacing Au for a non-noble-metal material, which would result in a dramatically decreased optical absorption cross section [40].

2. Time-dependent plasmonic heating

The time-dependent local temperatures of each nanomagnet in response to an optical excitation are simulated using three-dimensional finite-element thermal simulations using the “heat transfer module” of COMSOL. Thermal boundary conditions are implemented by meshing the glass substrate as a half-sphere with a radius of $12.5 \mu\text{m}$, which is 50 times the largest dimension of the nanoheaters (i.e., 250 nm). The temperature of the lower boundary of this half-sphere is set to 300 K. The amount of heat diffusing from the plasmonic heaters into the substrate is shown to be

little enough to be consistent with this choice of simulation volume and boundary condition.

The following values for the thermal conductivity k , thermal capacity C_p , and mass density ρ of all used materials, taken from tabulated values, are used.

	k ($\text{W m}^{-1}\text{K}^{-1}$)	C_p ($\text{J kg}^{-1}\text{K}^{-1}$)	ρ (kg m^{-3})
Gold	318	129	19 300
Nickel	70.2	456	8890
Permalloy	34.6	494	8740
Pyrex glass	1.4	730	2210

The time-dependent heat source density, which is equal to $\sigma_{\text{abs}}I/V$ with V the element's volume and I the light intensity, has been specified for each nanoheater, using the double-pulse laser profile $I(t)$ specified in Sec. V A of the main text, and the island- and polarization-dependent absorption cross sections $\sigma_{\text{abs}}(\lambda = 728 \text{ nm})$ shown in Fig. 8.

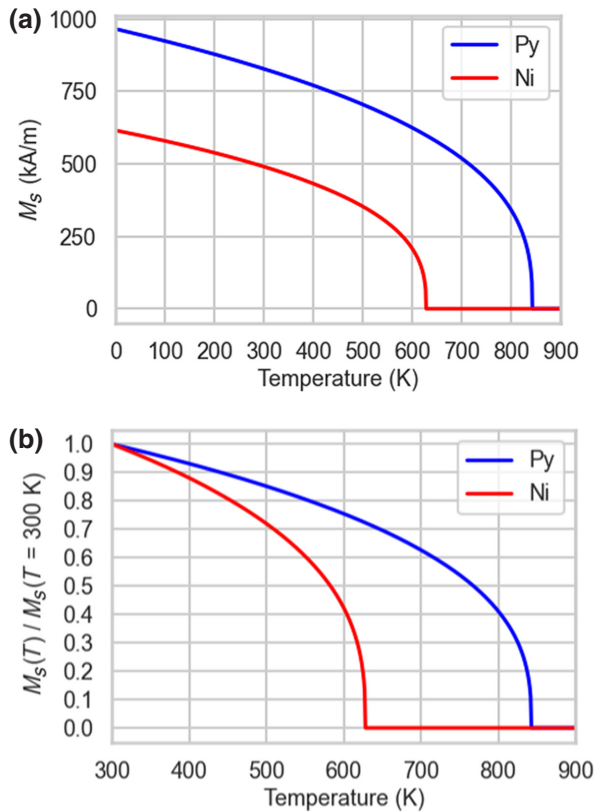


FIG. 9. Temperature dependence of the saturation magnetization for Ni (red) and Py (blue) shown (a) in absolute values and (b) with respect to the room-temperature value.

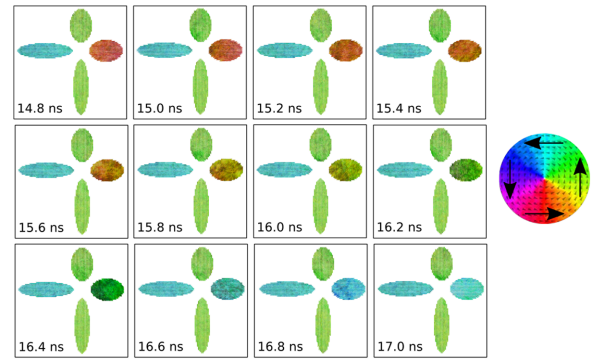


FIG. 10. Time-dependent snapshots of the AND gate with input configuration 01 [see the third column of Fig. 3(b)] obtained from micromagnetic simulations taken at time intervals of 0.2 ns. The continuous change of the magnetization orientation of the output island, represented by the colors of the color wheel, from red (at 14.8 ns) via green (at 16.2 ns) to cyan (at 17.0 ns), corroborates a coherent (counterclockwise) rotation of the net moment.

3. Temperature-dependent saturation magnetization

The saturation magnetization $M_s(T)$ as a function of temperature, calculated as described in the main text, is shown in Fig. 9(a) for Ni and Py. Nickel has a lower saturation magnetization and Curie temperature T_C compared to permalloy. Figure 9(b) compares the saturation magnetization $M_s(T)$ of each material to their respective value at room temperature $M_s(T = 300 \text{ K})$. It shows the more rapid relative reduction of the relative saturation magnetization in nickel, which at 600 K is only 42% of the room-temperature value, while permalloy retains 75% of $M_s(T = 300 \text{ K})$. In order to achieve a reduction to 40% of the saturation magnetization in permalloy, the temperature would need to be 200 K higher (i.e., about 800 K).

4. Coherent reversal

We use micromagnetic simulations to investigate how the reversals take place. Snapshots of the magnetization taken at time intervals of 0.2 ns indicate a coherent reversal, as shown in Fig. 10.

5. Functionally complete NML gate

Although both AND and OR logic can be implemented with the gate design of Fig. 2(a) thanks to the reconfigurability, it is insufficient to implement all Boolean functions by assembling a circuit of AND and OR gates. The reason for this shortcoming is the fact that the AND and OR gates do not possess the property of functional completeness, in contrast to the universal NAND gate. Here, we therefore elaborate on a design that can be used as a thermoplasmonic nanomagnetic NAND gate, with an operation mode controlled by the polarization-dependent plasmonic heating.

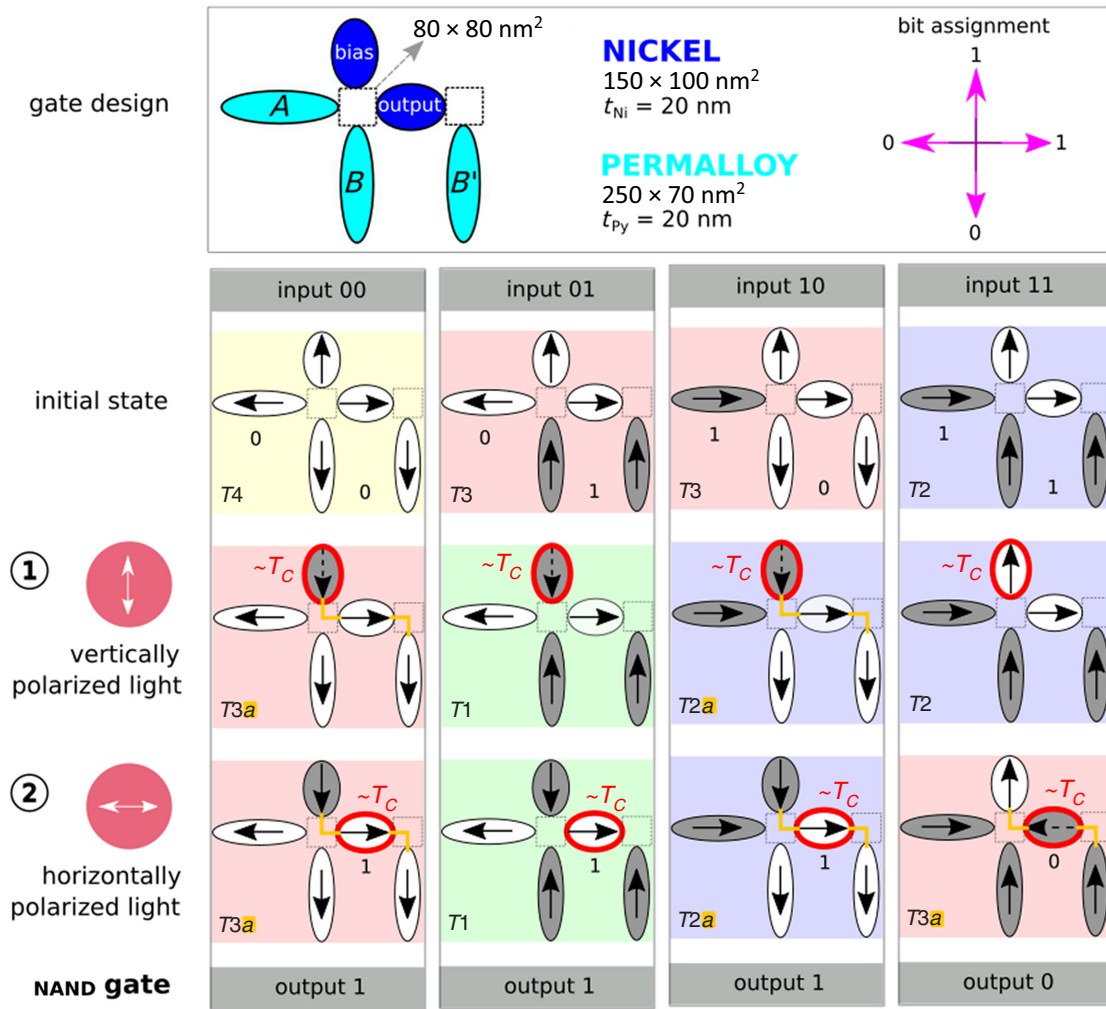


FIG. 11. Design and operating principle of a thermoplasmonic NAND gate. The same design is used as for the reconfigurable AND-OR gate, but with an additional island B' . This island lifts the energy hierarchy of single square ASI vertex to $E(T_4) > E(T_3) > E(T_2) > E(T_{3a}) > E(T_{2a}) > E(T_1)$. The label a refers to states for which the magnetization of the output islands is aligned with the stray fields of the bias island and island B' (indicated with an orange line).

As shown in Fig. 11, a NAND gate can be realized by adding an island B' to the design of the AND-OR gate. This additional island always has the same magnetization direction as input island B . The logical NAND behavior is achieved by illuminating the gate with a pulse of vertically polarized light and subsequently with a pulse of horizontally polarized light.

The design of this gate is found by a screening process, which only takes the initial field-set magnetic configuration and the sequence of heating pulses into account, due to the deterministic relaxation enabled by island-selective thermoplasmonic heating. A simple point-dipole interaction model allows us to explore the compatibility of the excited magnetic transitions with the desired logic functionality.

Because of the additional island, the energy hierarchy $E(T_4) > E(T_3) > E(T_2) > E(T_1)$ no longer strictly

applies. For input configuration 11 (fourth column of Fig. 11), a transition from T_2 to T_3 is energetically favorable: in the second step of the light protocol, the horizontal output island switches from a state for which its magnetization opposes the stray fields of the bias island and island B' to a state for which its magnetization aligns with these stray fields (labeled with a). The energy hierarchy $E(T_2) > E(T_{3a})$ also plays a role for input configuration 00 (first column of Fig. 11), where the horizontal output island does not switch when heated close to T_C . Because of the alignment with the stray fields of the bias island and island B' , the output magnetization keeps the direction corresponding to bit 1, as desired for a NAND gate with input 00.

The performance of the NAND gate shown in Fig. 11 has been tested for identical nanomagnet properties and MuMax3 simulation settings as in the main text, using

the same temperature profile for the vertical islands B and B' . To simulate the heating effect of a vertically polarized laser pulse (first step of the heating protocol), we must interchange the temperature profiles of the horizontal and vertical islands in Fig. 4(c), i.e., $T^A(t) \leftrightarrow T^B(t)$ and $T^{\text{output}}(t) \leftrightarrow T^{\text{bias}}(t)$, as the profiles of Fig. 4(c) are obtained with horizontally polarized light. For the second step of the heating protocol, we can directly use the profiles of Fig. 4(c).

Our micromagnetic simulations show success rates of 199/200, 200/200, and 198/200 for input configurations 00, 01, and 10, respectively. The performance for input configuration 11 is slightly lower (185/200) due to the smaller energy difference between the $T2$ and $T3a$ states. These results, already showing the potential of our operating mode, can be improved by optimizing the simple gate design of Fig. 11 (e.g., by modifying the island thickness).

-
- [1] Sasikanth Manipatruni, Dmitri E. Nikonov, and Ian A. Young, Beyond CMOS computing with spin and polarization, *Nat. Phys.* **14**, 338 (2018).
 - [2] Massimiliano Di Ventra and Fabio L. Traversa, Perspective: Memcomputing: Leveraging memory and physics to compute efficiently, *J. Appl. Phys.* **123**, 180901 (2018).
 - [3] Abu Sebastian, Manuel Le Gallo, Riduan Khaddam-Aljameh, and Evangelos Eleftheriou, Memory devices and applications for in-memory computing, *Nat. Nanotechnol.* **15**, 529 (2020).
 - [4] A. Ney, C. Pampuch, R. Koch, and K. H. Ploog, Programmable computing with a single magnetoresistive element, *Nature* **425**, 485 (2003).
 - [5] Jianguo Wang, Hao Meng, and Jian-Ping Wang, Programmable spintronics logic device based on a magnetic tunnel junction element, *J. Appl. Phys.* **97**, 10D509 (2005).
 - [6] Seungyeon Lee, Sunghoon Choa, Seungjun Lee, and Hyungsoon Shin, Magneto-logic device based on a single-layer magnetic tunnel junction, *IEEE Trans. Electron Devices* **54**, 2040 (2007).
 - [7] M. P. Kostylev, A. A. Serga, T. Schneider, B. Leven, and B. Hillebrands, Spin-wave logical gates, *Appl. Phys. Lett.* **87**, 153501 (2005).
 - [8] Thomas Schneider, Alexander A. Serga, Britta Leven, Burkard Hillebrands, Robert L. Stamps, and Mikhail P. Kostylev, Realization of spin-wave logic gates, *Appl. Phys. Lett.* **92**, 022505 (2008).
 - [9] Michael Balynskiy, Howard Chiang, David Gutierrez, Alexander Kozhevnikov, Yuriy Filimonov, and Alexander Khitun, Reversible magnetic logic gates based on spin wave interference, *J. Appl. Phys.* **123**, 144501 (2018).
 - [10] Anjan Barman, Gianluca Gubbiotti, Sam Ladak, Adekunle Olusola Adeyeye, Maciej Krawczyk, Joachim Gräfe, Christoph Adelman, Sorin Cotofana, Azad Naeemi, and Vitaliy I. Vasyuchka, *et al.*, The 2021 magnonics roadmap, *J. Phys.: Condens. Matter* **33**, 413001 (2021).
 - [11] D. A. Allwood, G. Xiong, C. C. Faulkner, D. Atkinson, D. Petit, and R. P. Cowburn, Magnetic domain-wall logic, *Science* **309**, 16881692 (2005).
 - [12] S. E. Barnes, J. Ieda, and S. Maekawa, Magnetic memory and current amplification devices using moving domain walls, *Appl. Phys. Lett.* **89**, 122507 (2006).
 - [13] J. H. Franken, H. J. M. Swagten, and B. Koopmans, Shift registers based on magnetic domain wall ratchets with perpendicular anisotropy, *Nat. Nanotechnol.* **7**, 499 (2012).
 - [14] Zhaochu Luo, Aleš Hrabec, Trong Phuong Dao, Giacomo Sala, Simone Finizio, Junxiao Feng, Sina Mayr, Jörg Raabe, Pietro Gambardella, and Laura J. Heyderman, Current-driven magnetic domain-wall logic, *Nature* **579**, 214 (2020).
 - [15] Xichao Zhang, G. P. Zhao, Hans Fangohr, J. Ping Liu, W. X. Xia, J. Xia, and F. J. Morvan, Skyrmion-skyrmion and skyrmion-edge repulsions in skyrmion-based racetrack memory, *Sci. Rep.* **5**, 1 (2015).
 - [16] R. P. Cowburn, Probing antiferromagnetic coupling between nanomagnets, *Phys. Rev. B* **65**, 092409 (2002).
 - [17] György Csaba, Alexandra Imre, Gary H. Bernstein, Wolfgang Porod, and Vitali Metlushko, Nanocomputing by field-coupled nanomagnets, *IEEE Trans. Nanotechnol.* **99**, 209 (2002).
 - [18] G. Csaba, A. Imre, G. H. Bernstein, W. Porod, and V. Metlushko, in *Nanotechnology, 2002. IEEE-NANO 2002. Proceedings of the 2002 2nd IEEE Conference on*, p. 59. IEEE, 2002.
 - [19] G. Csaba, P. Lugli, and W. Porod, in *Proc. of 4th IEEE Conf. on Nano*, p. 346, 2004.
 - [20] Alexandra Imre, G. Csaba, L. Ji, A. Orlov, G. H. Bernstein, and W. Porod, Majority logic gate for magnetic quantum-dot cellular automata, *Science* **311**, 205 (2006).
 - [21] Javier F. Pulecio, Pruthvi K. Pendru, Anita Kumari, and Sanjukta Bhanja, Magnetic cellular automata wire architectures, *IEEE Trans. Nanotechnol.* **10**, 1243 (2011).
 - [22] David B. Carlton, Brian Lambson, Andreas Scholl, Antony T. Young, Scott D. Dhuey, Paul D. Ashby, Eduard Tuchfeld, and Jeffrey Bokor, Computing in thermal equilibrium with dipole-coupled nanomagnets, *IEEE Trans. Nanotechnol.* **10**, 1401 (2011).
 - [23] Zheng Gu, Mark E. Nowakowski, David B. Carlton, Ralph Storz, Mi-Young Im, Jeongmin Hong, Weilun Chao, Brian Lambson, Patrick Bennett, Mohammad T. Alam, Matthew A. Marcus, Andrew Doran, Anthony Young, Andreas Scholl, Peter Fischer, and Jeffrey Bokor, Sub-nanosecond signal propagation in anisotropy-engineered nanomagnetic logic chains, *Nat. Commun.* **6**, 1 (2015).
 - [24] Hanu Arava, Peter M. Derlet, Jaianth Vijayakumar, Jizhai Cui, Nicholas S. Bingham, Armin Kleibert, and Laura J. Heyderman, Computational logic with square rings of nanomagnets, *Nanotechnology* **29**, 265205 (2018).
 - [25] Pieter Gypens, Jonathan Leliaert, and Bartel Van Waeyenberge, Balanced Magnetic Logic Gates in a Kagome Spin Ice, *Phys. Rev. Appl.* **9**, 034004 (2018).
 - [26] Hanu Arava, Naëmi Leo, Dominik Schildknecht, Jizhai Cui, Jaianth Vijayakumar, Peter M. Derlet, Armin Kleibert, and Laura J. Heyderman, Engineering Relaxation Pathways in Building Blocks of Artificial Spin Ice for Computation, *Phys. Rev. Appl.* **11**, 054086 (2019).

- [27] Francesco Caravelli and Cristiano Nisoli, Logical gates embedding in artificial spin ice, *New J. Phys.* **22**, 103052 (2020).
- [28] M. Niemier, M. Alam, Xiaobo Sharon Hu, G. Bernstein, Wolfgang Porod, M. Putney, and J. DeAngelis, in *Proceedings of the 2007 international symposium on Low power electronics and design*, p. 26. ACM, (2007).
- [29] Mohammad Tanvir Alam, Mohammad Jafar Siddiq, Gary H. Bernstein, Michael Niemier, Wolfgang Porod, and Xiaobo Sharon Hu, On-chip clocking for nanomagnetic logic devices, *IEEE Trans. Nanotechnol.* **9**, 348 (2010).
- [30] E. Varga, G. Csaba, G. H. Bernstein, and W. Porod, Domain-wall assisted switching of single-domain nanomagnets, *IEEE Trans. Magn.* **48**, 3563 (2012).
- [31] Debanjan Bhowmik, Long You, and Sayeef Salahuddin, Spin Hall effect clocking of nanomagnetic logic without a magnetic field, *Nat. Nanotechnol.* **9**, 59 (2014).
- [32] Jayasimha Atulasimha and Supriyo Bandyopadhyay, Bennett clocking of nanomagnetic logic using multiferroic single-domain nanomagnets, *Appl. Phys. Lett.* **97**, 173105 (2010).
- [33] Noel D'Souza, Mohammad Salehi Fashami, Supriyo Bandyopadhyay, and Jayasimha Atulasimha, Experimental clocking of nanomagnets with strain for ultralow power Boolean logic, *Nano Lett.* **16**, 1069 (2016).
- [34] Rolf Landauer, Irreversibility and heat generation in the computing process, *IBM J. Res. Dev.* **5**, 183 (1961).
- [35] Mohammad Salehi Fashami, Kamaram Munira, Supriyo Bandyopadhyay, Avik W. Ghosh, and Jayasimha Atulasimha, Switching of dipole coupled multiferroic nanomagnets in the presence of thermal noise: Reliability of nanomagnetic logic, *IEEE Trans. Nanotechnol.* **12**, 1206 (2013).
- [36] Kamaram Munira, Yunkun Xie, Souheil Nadri, Mark B. Forgues, Mohammad Salehi Fashami, Jayasimha Atulasimha, Supriyo Bandyopadhyay, and Avik W. Ghosh, Reducing error rates in straintronic multiferroic nanomagnetic logic by pulse shaping, *Nanotechnology* **26**, 245202 (2015).
- [37] Santhosh Sivasubramani, Venkat Mattela, Chandrajit Pal, and Amit Acharyya, Dipole coupled magnetic quantum-dot cellular automata-based efficient approximate nanomagnetic subtractor and adder design approach, *Nanotechnology* **31**, 025202 (2019).
- [38] David Carlton, Brian Lambson, Andreas Scholl, Anthony Young, Paul Ashby, Scott Dhuey, and Jeffrey Bokor, Investigation of defects and errors in nanomagnetic logic circuits, *IEEE Trans. Nanotechnol.* **11**, 760 (2012).
- [39] Matteo Pancaldi, Naëmi Leo, and Paolo Vavassori, Selective and fast plasmon-assisted photo-heating of nanomagnets, *Nanoscale* **11**, 7656 (2019).
- [40] Guillaume Baffou and Romain Quidant, Thermo-plasmonics: Using metallic nanostructures as nano-sources of heat, *Laser Photon. Rev.* **7**, 171 (2013).
- [41] Stefan Alexander Maier, *Plasmonics: Fundamentals and Applications* (Springer Science & Business Media, New York, 2007).
- [42] Nicolò Maccaferri, Juan B. González-Díaz, Stefano Bonetti, Andreas Berger, Mikko Kataja, Sebastiaan Van Dijken, Josep Nogués, Valentina Bonanni, Zhaleh Pirzadeh, Alexandre Dmitriev, Johan Åkerman, and Paolo Vavassori, Polarizability and magnetoplasmonic properties of magnetic general nanoellipsoids, *Opt. Express* **21**, 9875 (2013).
- [43] Nicolò Maccaferri, Luca Bergamini, Matteo Pancaldi, Mikolaj K. Schmidt, Mikko Kataja, Sebastiaan van Dijken, Nerea Zabala, Javier Aizpurua, and Paolo Vavassori, Anisotropic nanoantenna-based magnetoplasmonic crystals for highly enhanced and tunable magneto-optical activity, *Nano Lett.* **16**, 2533 (2016).
- [44] R. F. Wang, C. Nisoli, R. S. Freitas, J. Li, W. McConville, B. J. Cooley, M. S. Lund, N. Samarth, C. Leighton, V. H. Crespi, and P. Schiffer, Artificial 'spin ice' in a geometrically frustrated lattice of nanoscale ferromagnetic islands, *Nature* **439**, 303 (2006).
- [45] J. M. D. Coey, *Magnetism and Magnetic Materials* (Cambridge Univ. Press, New York, NY, 2010).
- [46] COMSOL Multiphysics®v. 5.4. www.comsol.com. COMSOL AB, Stockholm, Sweden.
- [47] A. Vansteenkiste, J. Leliaert, M. Dvornik, M. Helsen, F. Garcia-Sanchez, and B. Van Waeyenberge, The design and verification of MuMax3, *AIP Adv.* **4**, 107133 (2014).
- [48] Jonathan Leliaert, Jeroen Mulkers, Jonas De Clercq, Annelies Coene, M. Dvornik, and Bartel Van Waeyenberge, Adaptively time stepping the stochastic Landau-Lifshitz-Gilbert equation at nonzero temperature: Implementation and validation in MuMax3, *AIP Adv.* **7**, 125010 (2017).
- [49] J. M. Porro, A. Bedoya-Pinto, A. Berger, and P. Vavassori, Exploring thermally induced states in square artificial spin-ice arrays, *New J. Phys.* **15**, 055012 (2013).
- [50] Using Poisson statistics of small numbers with an average error rate of $\lambda = 5$ per 200 simulations, we can calculate the probability $P(X = k) = (\lambda^k/k!) \exp(-\lambda)$ of having k unsuccessful switching events when simulating 200 times. For AND 01* and OR 10*, this probability is $P(X = 8) = 6.5\%$ and $P(X = 2) = 8.4\%$, respectively. These numbers are plausible compared to $P(X = \lambda) = 17.5\%$.
- [51] Louis Néel, Théorie du traînage magnétique des ferromagnétiques en grains fins avec applications aux terres cuites, *Ann. Géophys.* **5**, 99 (1949).
- [52] W. F. Brown, Relaxational behavior of fine magnetic particles, *J. Appl. Phys.* **30**, S130 (1959).
- [53] Sabri Koraltan, Matteo Pancaldi, Naëmi Leo, Claas Abert, Christoph Vogler, Kevin Hofhuis, Florian Slanovc, Florian Bruckner, Paul Heistracher, Matteo Menniti, Paolo Vavassori, and Dieter Suess, Dependence of energy barrier reduction on collective excitations in square artificial spin ice: A comprehensive comparison of simulation techniques, *Phys. Rev. B* **102**, 064410 (2020).
- [54] Naëmi Leo, Matteo Pancaldi, Sabri Koraltan, Pedro Villalba González, Claas Abert, Christoph Vogler, Florian Slanovc, Florian Bruckner, Paul Heistracher, Kevin Hofhuis, Matteo Menniti, Dieter Suess, and Paolo Vavassori, Chiral switching and dynamic barrier reductions in artificial square ice, *New J. Phys.* **23**, 033024 (2021).
- [55] I. R. B. Ribeiro, F. S. Nascimento, S. O. Ferreira, W. A. Moura-Melo, C. A. R. Costa, J. Borme, P. P. Freitas, G. M. Wysin, C. I. L. De Araujo, A. R. Pereira, Realization of rectangular artificial spin ice and direct observation of high energy topology, *Sci. Rep.* **7**, 1 (2017).

- [56] F. S. Nascimento, L. A. S. Mól, W. A. Moura-Melo, and A. R. Pereira, From confinement to deconfinement of magnetic monopoles in artificial rectangular spin ices, *New J. Phys.* **14**, 115019 (2012).
- [57] The average energy per bit-write can be calculated as the average power consumption divided by the average writing speed. For the 2.5" *BarraCuda (5 TB)*, this yields $(2.1 \text{ W})/(140 \text{ MB/s}) = 15 \text{ nJ}$.
- [58] Hikaru Nomura, Taishi Furuta, Kazuki Tsujimoto, Yuki Kuwabiraki, Ferdinand Peper, Eiiti Tamura, Shinji Miwa, Minoru Goto, Ryoichi Nakatani, and Yoshishige Suzuki, Reservoir computing with dipole-coupled nanomagnets, *Jpn. J. Appl. Phys.* **58**, 070901 (2019).
- [59] J. H. Jensen and G. Tufte, Reservoir computing in artificial spin ice, *Artif. Life Conf. Proc.* **32**, 376 (2020).
- [60] Kwan Hon, Yuki Kuwabiraki, Minoru Goto, Ryoichi Nakatani, Yoshishige Suzuki, and Hikaru Nomura, Numerical simulation of artificial spin ice for reservoir computing, *Appl. Phys. Express* **14**, 033001 (2021).
- [61] Jack C. Gartside, Kilian D. Stenning, Alex Vanstone, Holly H. Holder, Daan M. Arroo, Troy Dion, Francesco Caravelli, Hidekazu Kurebayashi, and Will R. Branford, Reconfigurable training and reservoir computing in an artificial spin-vortex ice via spin-wave fingerprinting, *Nat. Nanotechnol.* **17**, 460 (2022).
- [62] Francesco Caravelli, Gia-Wei Chern, and Cristiano Nisoli, Artificial spin ice phase-change memory resistors. *New J. Phys.* **24**, 023020 (2022).
- [63] Kerem Yunus Camsari, Sayeef Salahuddin, and Supriyo Datta, Implementing p-bits with embedded MTJ, *IEEE Electron Device Lett.* **38**, 1767 (2017).
- [64] William A. Borders, Ahmed Z. Pervaiz, Shunsuke Fukami, Kerem Y. Camsari, Hideo Ohno, and Supriyo Datta, Integer factorization using stochastic magnetic tunnel junctions, *Nature* **573**, 390 (2019).
- [65] Pieter Gypens, Bartel Van Waeyenberge, Massimiliano Di Ventra, Jonathan Leliaert, and Daniele Pinna, Nanomagnetic Self-Organizing Logic Gates, *Phys. Rev. Appl.* **16**, 024055 (2021).
- [66] Peter B. Johnson and R.-W. Christy, Optical constants of the noble metals, *Phys. Rev. B* **6**, 4370 (1972).
- [67] Š. Višňovský, V. Pařízek, M. Nývlt, P. Kielar, V. Prosser, and R. Krishnan, Magneto-optical Kerr spectra of nickel, *J. Magn. Magn. Mater.* **127**, 135 (1993).
- [68] Mikhail N. Polyanskiy, Refractive index database. <https://refractiveindex.info>. Accessed on 2021-09-28.